

Monolayer Nanosheets with an Extremely High Drug Loading toward Controlled Delivery and Cancer Theranostics

Liuqi Peng, Xuan Mei, Jun He, Jiekun Xu, Weiku Zhang,* Ruizheng Liang,* Min Wei,* David G. Evans, and Xue Duan

2D nanomaterials have attracted considerable research interest in drug delivery systems, owing to their intriguing quantum size and surface effect. Herein, Gd³⁺-doped monolayered-double-hydroxide (MLDH) nanosheets are prepared via a facile bottom-up synthesis method, with a precisely controlled composition and uniform morphology. MLDH nanosheets as drug carrier are demonstrated in co-loading of doxorubicin and indocyanine green (DOX&ICG), with an ultrahigh drug loading content (LC) of 797.36% and an encapsulation efficiency (EE) of 99.67%. This is, as far as it is known, the highest LC level at nearly 100% of EE among previously reported 2D drug delivery systems so far. Interestingly, the as-prepared DOX&ICG/MLDH composite material shows both pH-controlled and near-infrared-irradiation-induced DOX release, which holds a promise in stimulated drug release. An *in vivo* dual-mode imaging, including near-infrared fluorescence and magnetic resonance imaging, enables a noninvasive visualization of distribution profiles at the tumor site. In addition, *in vitro* and *in vivo* therapeutic evaluations demonstrate an excellent trimode synergetic anticancer activity and superior biocompatibility of DOX&ICG/MLDH. Therefore, MLDH nanosheets provide new perspectives in the design of multifunctional nanomedicine, which shows promising applications in controlled drug delivery and cancer theranostics.

Recently, a number of 2D nanomaterials have attracted considerable research interest in biomedicine, owing to their fascinating quantum size and surface effect.^[1–6] For instance, graphene,^[7] transition-metal dichalcogenides (TMDs),^[8] hexagonal boron nitride (h-BN),^[9] and black phosphorus (BP)^[10] with an ultrathin structure, have been explored as carriers for drug loading, which

L. Peng, X. Mei, Dr. R. Liang, Prof. M. Wei, Prof. D. G. Evans, Prof. X. Duan
State Key Laboratory of Chemical Resource Engineering
Beijing Advanced Innovation Center for Soft Matter
Science and Engineering
Beijing University of Chemical Technology
Beijing 100029, P. R. China
E-mail: liangrz@mail.buct.edu.cn, liangruizheng2000@163.com;
weimin@mail.buct.edu.cn

Dr. J. He, Dr. W. Zhang
Institute of Clinical Medical Sciences & Department
of Pharmacy China-Japan Friendship Hospital
Beijing 100029, P. R. China
E-mail: zhangweiku@zryhy.com.cn, cpuzwk@163.com

Dr. J. Xu
School of Life Sciences
Beijing University of Chinese Medicine
Beijing 100029, P. R. China

DOI: 10.1002/adma.201707389

have shown excellent performances in cancer therapy. Moreover, some 2D nanomaterials (e.g., graphene, TMDs, and BP) with a strong near-infrared (NIR) optical absorption can serve as photothermal or photodynamic agents, which combine with drugs to realize synergistic treatment.^[11–17] However, the previously reported ultrathin 2D nanomaterials are mainly based on a “top-down” mechanical-exfoliation strategy, which show difficulties in the control over particle size, thickness, morphology, and uniformity.^[18–21] Moreover, 2D nanomaterials normally suffer from a low drug loading content (LC) and encapsulation efficiency (EE), if the fine structure and drug-carrier interaction cannot be elaborately regulated. This would lead to some potential safety issue and the loss of valuable drugs. Therefore, how to develop new drug formulation on the basis of 2D nanomaterial design and synthesis exploration, so as to achieve controlled structure and largely enhanced loading capacity toward cancer therapy, still remains a big challenge.

As a typical class of 2D nanomaterial, layered double hydroxides (LDHs) can be expressed as $[M^{2+}_{1-x}M^{3+}_x(OH)_2](A^{n-})_{x/n} \times mH_2O$, where M²⁺ and M³⁺ are di- and trivalent metal cations distributed in edge-sharing MO₆ octahedra host layer, and Aⁿ⁻ is an exchangeable interlayer anion.^[22–26] Due to the unique 2D structure with the versatility in both host layer and interlayer anion, LDHs nanomaterials have been extensively studied in drug delivery systems for controlled release of genes and drugs, which showed advantages of biocompatibility and passive targeting.^[27–29] Despite of the progress of LDHs bulk materials in biomedicine applications,^[30,31] LDHs ultrathin nanosheets as a multimodal theranostic delivery carrier have not been demonstrated. This is because the “top-down” mechanical-exfoliation method from bulk LDHs gives a rather low efficiency and involves deleterious organic reagents.^[32] From the viewpoint of practical application, exploration on a “bottom-up” strategy for the synthesis of LDHs ultrathin nanosheets, would endow this carrier with a finely controlled structure (e.g., chemical composition, uniform size/morphology, high specific surface area) and the resulting superior functionality.

Herein, we designed and prepared Gd³⁺-doped monolayered-double-hydroxide (MLDH) nanosheets via a new bottom-up synthesis method, which were employed in dual-mode cancer

imaging and synergistic therapy. X-ray diffraction (XRD), atomic force microscopy (AFM), and high-resolution transmission electron microscopy (HRTEM) show that MLDH nanosheets possess a uniform lateral size of ≈ 70 nm and a thickness of ≈ 1.2 nm. Most interestingly, MLDH nanosheets as drug carrier can achieve the coloaded of doxorubicin hydrochloride (DOX, chemotherapeutics drug) and indocyanine green (ICG, photothermal and photodynamic agent), with an ultrahigh drug LC of 797.36% and an EE of 99.67%. This is, to the best of our knowledge, the highest LC level at nearly 100% of EE among reported 2D drug delivery systems so far.^[33–38] The as-prepared DOX&ICG/MLDH nanocomposite material shows both pH-controlled and NIR-irradiation-induced DOX release, as well as significantly large reactive oxygen species (ROS) production. This drug formulation demonstrates a trimode combination therapy including chemo, photothermal therapy (PTT), and photodynamic therapy (PDT) based on in vitro tests, which exhibits an excellent synergetic anticancer activity and superior biocompatibility. In addition, in vivo near infrared fluorescence (NIRF) and magnetic resonance (MR) imaging studies reveal an enhanced uptake of DOX&ICG/MLDH at tumor site; in vivo therapy investigations exhibit dramatically strong ability toward tumor elimination.

Figure 1a illustrates the schematic procedure for the fabrication of MLDH-based drug delivery system toward efficient loading and precisely controlled delivery of theranostic agents. Gd-containing MLDH nanosheets were prepared through a new “bottom-up” method, in which Gd^{3+} was introduced in MLDH host layers (mass content: 5%) so as to realize magnetic resonance imaging (MRI). HRTEM imaging of MLDH nanosheets shows a monodispersed sheet structure with a lateral size of ≈ 70 nm (Figure 1b). Moreover, the elemental distribution of MLDH nanosheets was studied by energy-dispersive X-ray (EDX) spectroscopy. Both the elemental-mapping analysis (Figure S1a, Supporting Information) and EDX line profile (Figure S1b, Supporting Information) reveal that Mg, Al, and Gd atoms are homogeneously distributed throughout the MLDH nanosheet, indicating that Gd is successfully doped into MLDH host layers. The thickness of MLDH nanosheets is determined to be ≈ 1.2 nm by AFM (Figure 1c,d), close to the value reported from mechanical delamination method.^[39] The equivalent hydrodynamic diameter of MLDH nanosheets is measured to be 70 ± 9.5 nm in water, phosphate buffer saline (PBS) and culture medium (Figure 1e), according to dynamic light scattering technique. The zeta potential of MLDH nanosheets is positive (43.2 ± 0.5 mV) in the three media, indicating a good stability (Figure S2, Supporting Information). We further investigate the structural information of MLDH nanosheets through XRD analysis. The bulk LDHs sample shows a typical (003) reflection of LDHs phase at $2\theta = 12.19^\circ$ (Figure 1f; green line). However, this is not observed for the MLDHs colloid sample (Figure 1f; red line), indicating the lack of long-range-ordered layered structure.^[40–42] As the colloid MLDH sample is dried, a restacking of monolayer nanosheets to bulk material would occur so as to decrease the total system energy, which is demonstrated by the appearance of 2θ reflection at 12.15° (Figure 1f; violet line). The X-ray photoelectron spectroscopy (XPS) shows the characteristic peak of Gd 4d at 143.8 eV ($4d_{5/2}$) and 149.0 eV ($4d_{3/2}$) (Figure 1g), indicating a successful doping of Gd^{3+} into

MLDH laminate. For a MRI contrast agent, T_1 -weighted relaxivity (r_1) is a key parameter in MRI properties evaluation.^[43–45] The r_1 value of DOX&ICG/MLDH was determined to be $7.93 \times 10^{-3} \text{ M}^{-1} \text{ s}^{-1}$ (Figure S3, Supporting Information) based on a pharmscan Magnetom Trio system with a 0.5 T magnetic field, which is ≈ 2.27 fold larger than that of commercial gadolinium-diethylenetriaminepentaacetic acid contrast agent ($\approx 3.5 \times 10^{-3} \text{ M}^{-1} \text{ s}^{-1}$).

After the loading of DOX and ICG, the uniform plate-like morphology of DOX&ICG/MLDH is well maintained with a lateral size of ≈ 80 nm, as revealed by HRTEM (Figure S4, Supporting Information). However, the thickness increases from ≈ 1.2 to ≈ 2.0 nm compared with pristine MLDH, as a result of the conjunction of DOX and ICG (Figure S5, Supporting Information). The drug loading is further confirmed by Fourier transform infrared spectroscopy (Figure S6, Supporting Information). Bands at 1582 cm^{-1} (stretching vibration of C=O) of DOX and 1427 cm^{-1} (stretching vibration of C=C) of ICG are observed, accompanied with the characteristic band of MLDH at 1354 cm^{-1} (vibration absorption peak of C=O), which indicates the drugs of DOX and ICG are successfully loaded onto MLDH nanosheets. In addition, the DOX&ICG/MLDH nanocomposite sample is highly stable in deionized water, PBS, and culture medium with nearly unaltered size distribution (Figure S7, Supporting Information). The hydrodynamic size of DOX&ICG/MLDH in these three media was monitored for one week, and no obvious change was found (Figure S8, Supporting Information), demonstrating a satisfactory storage stability. The Tyndall effect (Figure S9, Supporting Information) also verifies a high aqueous stability and dispersibility of both MLDH and DOX&ICG/MLDH samples.

By virtue of the ultrahigh specific surface area of MLDH nanosheets (with a theoretical value of $1534 \text{ m}^2 \text{ g}^{-1}$), its loading performance toward DOX and ICG was studied. The specific surface area of MLDH powdered sample is $488.65 \text{ m}^2 \text{ g}^{-1}$ (Figure S10, Supporting Information), which is lower than the theoretical value (calculated based on colloidal monolayer sample). This is owing to the accumulation of MLDH nanosheets during the drying process. For separate loading of DOX or ICG at adsorption balance, the LC of DOX and ICG are 344.56% and 227.88% while the EE of DOX and ICG are 85.41% and 55.82% with a mass ratio of drug:MLDH = 1:0.25 (Figure 2a,b). Subsequently, we investigated the coloaded of DOX and ICG (mass ratio of 1:1) onto the MLDH nanosheets. It is surprising that the coloaded efficiency is obviously enhanced compared with individual loading: the LC and EE value increase to as high as 797.36% and 99.67%, respectively, with a mass ratio of (DOX&ICG):MLDH = 1:0.125 (Figure 2c). This is the highest LC level at nearly 100% of EE among previously reported 2D drug delivery systems so far.^[33–38] The coloaded performance with various mass ratios of DOX:ICG is also investigated, and the results show that the optimal LC value (797.36%) can be obtained with DOX:ICG = 1:1 (Figure 2d: 455.28% and 490.42% for DOX:ICG = 1:2 and 2:1, respectively). Moreover, the EE value also follows a similar change tendency (Figure S11, Supporting Information). The results above indicate that a coupling of DOX molecule and ICG molecule occurs during the immobilization process, which may originate from the electrostatic interaction between

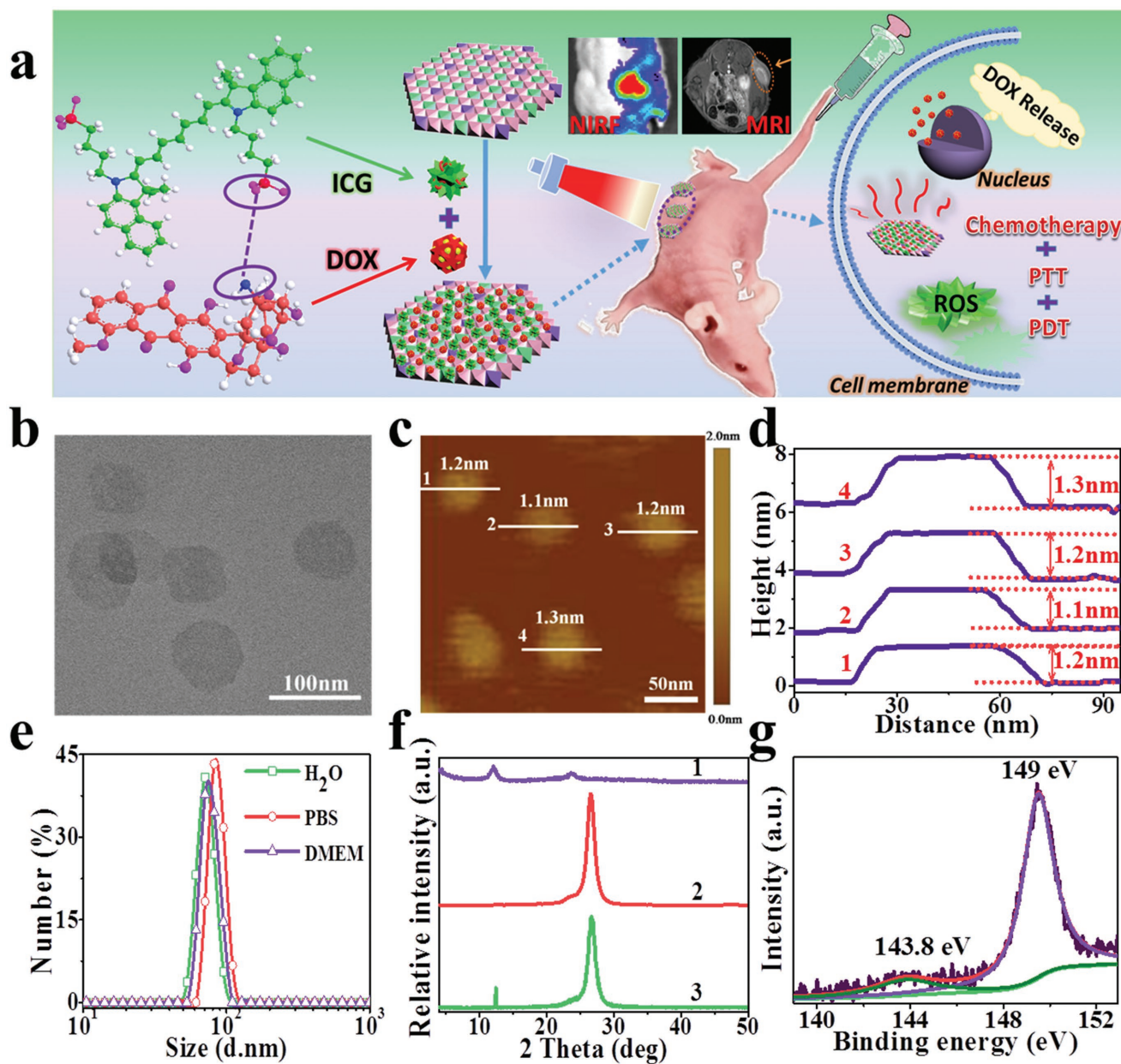


Figure 1. a) A schematic illustration for MLDH-based drug delivery system toward efficient loading and precisely controlled delivery of theranostic agents. b) HRTEM image of MLDH nanosheets. c) AFM image and d) measured thickness of MLDH nanosheets. e) Size distribution of MLDH nanosheets in water, PBS, and culture medium (high glucose Dulbecco's modified Eagle medium (DMEM)). f) XRD patterns of: (1) bulk LDH colloid, (2) MLDH nanosheets colloid, and (3) the restacking sample of MLDH nanosheets. The peak at 26.2° is ascribed to the PET film substrate. g) XPS spectra of MLDH nanosheets sample.

primary amine group in DOX and sulfonate group in ICG.^[46,47] The adsorption curves of MLDH toward DOX, ICG, and DOX&ICG were further studied (Figure 2e; Figure S12, Supporting Information). An ultrafast adsorption behavior is found within the first 1 min, with the increase of LC value to 244.89% (DOX), 214.76% (ICG), and 715.68% (DOX&ICG), respectively, followed by a gentle increment until the adsorption balance at 30 min. To reveal the interaction between DOX–ICG and drug–MLDH, isothermal titration calorimetry measurements were performed. The thermodynamic parameter shows that

both the DOX–ICG and DOX&ICG–MLDH system are autonomous ($\Delta G < 0$). In these two cases, the entropy change (ΔS) and enthalpy change (ΔH) are both negative, indicating the existence of Van der Waals' force, electrostatic interaction, or hydrogen bonding^[48–50] between DOX and ICG as well as between DOX&ICG and MLDH (Figure 2f; Figure S13, Supporting Information). The MLDH formulation reported here possesses two unique properties that account for the ultrahigh drug loading: (1) monolayer structure with an ultrahigh specific surface area; (2) a combined electrostatic interaction between

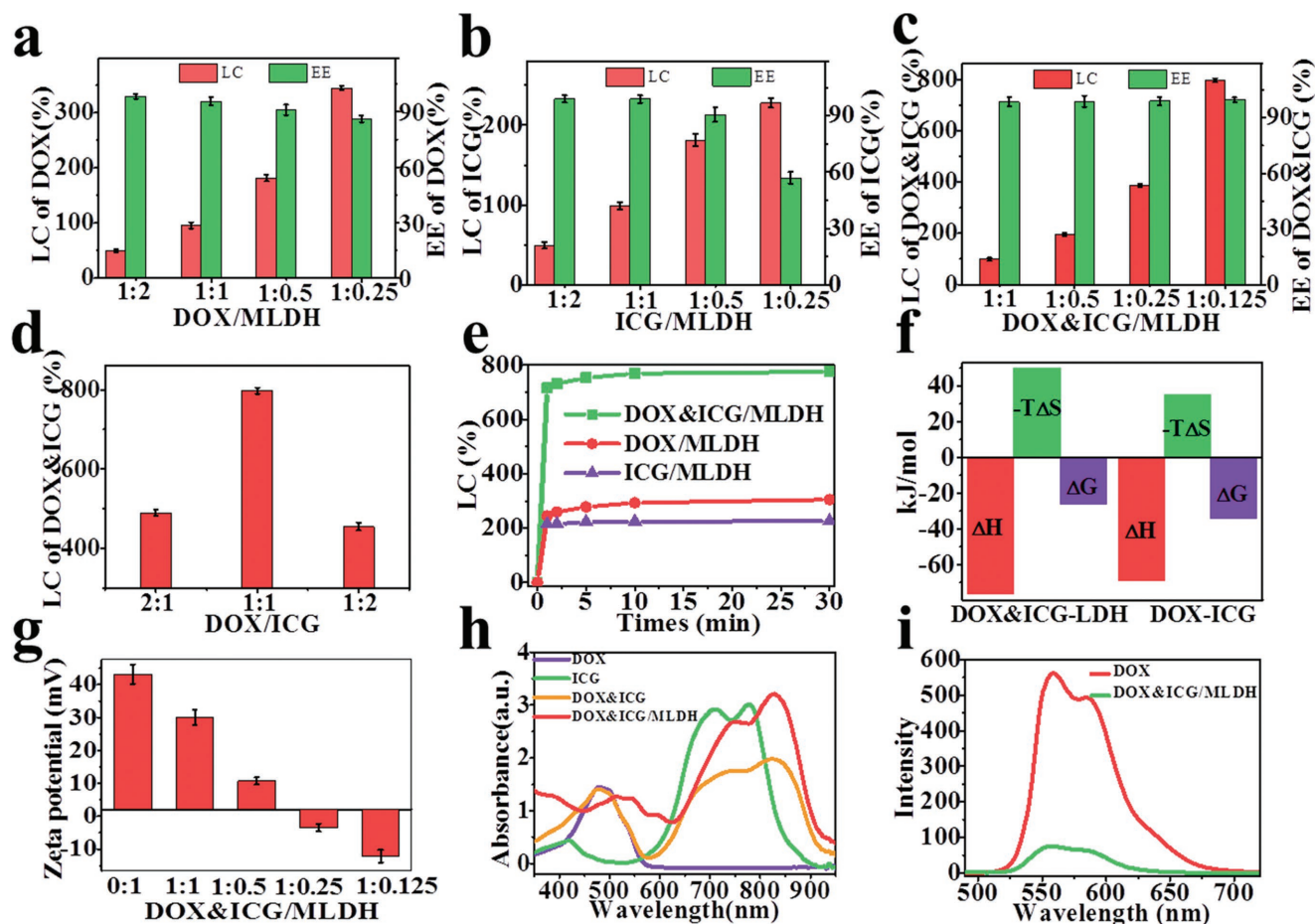


Figure 2. LC and EE of: a) DOX, b) ICG, and c) DOX&ICG onto MLDH nanosheets with various mass ratios. d) LC of DOX&ICG onto MLDH nanosheets with various mass ratios of DOX:ICG. e) Adsorption curves of DOX, ICG, and DOX&ICG onto MLDH nanosheets. f) Thermodynamic parameters ΔH , $-T\Delta S$, and ΔG for the DOX-ICG and DOX&ICG-MLDH system, respectively. g) Surface zeta potential of DOX&ICG/MLDH with various mass ratios of DOX&ICG:MLDH. h) UV-vis-NIR spectra of DOX, ICG, DOX&ICG, and DOX&ICG/MLDH, respectively. i) Fluorescence spectra of DOX and DOX&ICG/MLDH.

drug and MLDH nanosheets. The electrostatic interaction between DOX and ICG induces an integration with decreased system enthalpy and entropy (negative values of ΔH and ΔS , as shown in Figure 2f), accounting for the spontaneous adsorption of DOX&ICG onto the surface of MLDH nanosheets. Thus, a double-interaction mechanism is proposed in this drug loading system: DOX-ICG interaction and DOX&ICG-MLDH interaction provide additional decrease in system Gibbs free energy, resulting in an extremely high LC and EE. The zeta potential of MLDH nanosheets decreases from +43.3 to -12.2 mV after the drug loading (Figure 2g), which is ascribed to the immobilization of negatively charged DOX&ICG (-28.7 mV) onto positively charged MLDH nanosheets (+43.3 mV, Figure S14, Supporting Information). The UV-vis-NIR spectrum of DOX&ICG/MLDH sample displays a red-shift of both DOX and ICG relative to pristine DOX and ICG (Figure 2h), resulting in an obvious absorption enhancement at 808 nm. This facilitates the photothermal conversion property of DOX&ICG/MLDH in comparison with pristine ICG. In addition, the fluorescence intensity of DOX&ICG/LDH is obviously weaker than that of pristine DOX at the same DOX

concentration (Figure 2i), which is ascribed to the interaction among DOX, ICG, and MLDH nanosheets.

Since ICG possesses a strong NIR optical absorption and can realize an efficient photothermal conversion, the photothermal performance of DOX&ICG/MLDH was studied. The DOX&ICG/MLDH sample and control samples were irradiated by 808 nm laser with a power density of 1.5 W cm^{-2} . As shown in Figure 3a, the temperature of the DOX&ICG/MLDH suspension (concentration: $10 \mu\text{g mL}^{-1}$) increases by $33.68 \text{ }^\circ\text{C}$ within 3 min irradiation. In comparison, the control samples including PBS, culture medium, DOX suspension, and MLDH suspension only give a temperature increment of less than $3 \text{ }^\circ\text{C}$; while the ICG suspension shows an enhancement of $27.49 \text{ }^\circ\text{C}$. The thermal imaging photographs also reveal a clear visual observation for the temperature change (Figures S15a and S16, Supporting Information). The photostability tests over DOX&ICG/MLDH and pristine ICG were performed: pristine ICG shows a significant temperature decrease after five cycles; while DOX&ICG/MLDH maintains an enhanced photothermal performance compared with pristine ICG (Figure 3b). Subsequently, the photothermal effect as a function

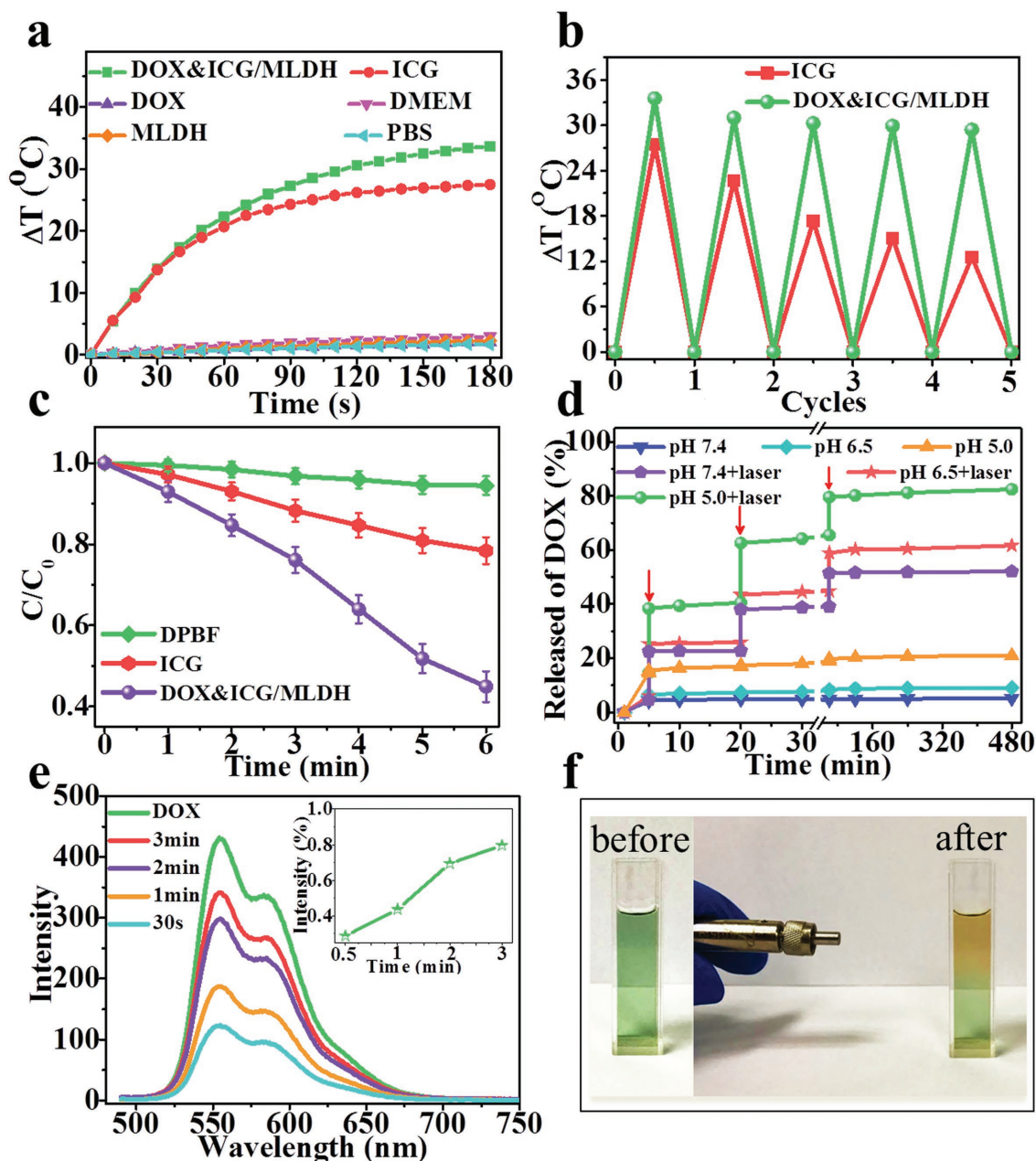


Figure 3. a) Photothermal effect of DOX&ICG/MLDH under 808 nm irradiation (1.5 W cm^{-2}), with ICG, DOX, DMEM, MLDH, and PBS used as control samples. b) Photostability tests of DOX&ICG/MLDH and ICG for five cycles. c) Normalized absorbance of the DPBF in the presence of ICG, DOX&ICG/MLDH, and blank sample under 808 nm laser irradiation (1.5 W cm^{-2}). d) DOX release from DOX&ICG/MLDH in PBS at pH 5.0, 6.5, and 7.4 with or without 808 nm irradiation (1.5 W cm^{-2}); the arrow indicates the time point of laser irradiation. e) Fluorescence intensity of free DOX solution ($10 \mu\text{g mL}^{-1}$) and the supernatant of DOX&ICG/MLDH after laser irradiation for 30 s, 1 min, 2 min, and 3 min; the inset shows the release percentage versus time. f) Photographs of the DOX&ICG/MLDH suspension before and after NIR laser irradiation.

of drug concentration (5, 10, and $20 \mu\text{g mL}^{-1}$) was investigated (Figure S17a, Supporting Information). The final temperature of DOX&ICG/MLDH suspension increases by 24.82, 33.68, and $42.07 \text{ }^\circ\text{C}$ (thermal imaging photographs in Figure S15 in the Supporting Information), respectively, superior to pristine ICG with the same concentration. The control over power density of 1.0 W cm^{-2} also gives a similar result (Figure S17b, Supporting Information). In addition, the photodynamic performance of

DOX&ICG/MLDH was studied based on the intrinsic property of ICG, by using 1,3-diphenylisobenzofuran (DPBF) as a probe to measure the ROS production^[51] (Figure 3c; Figure S18, Supporting Information). The DOX&ICG/MLDH sample gives an ROS production of 0.55 in the standard absorbance within 6 min NIR irradiation, much larger than pristine ICG (0.21). This would endow DOX&ICG/MLDH with a trimodal combination therapy including chemo, PTT, and PDT. Finally, the

storage stability tests reveal that the UV–vis–NIR absorption of DOX&ICG/MLDH only displays a slight decrease (less than 5%) while pristine ICG shows an obvious photobleaching after a 4 d storage at room temperature under daylight (Figure S19, Supporting Information), indicating a greatly improved stability of ICG upon loading onto MLDH nanosheets.

It has been recognized that an effective chemotherapy of DOX is dependent on its controlled release;^[47,52] thus, the release behavior of DOX from DOX&ICG/MLDH was studied with external stimuli (e.g., pH and NIR laser irradiation), by recording the UV absorbance at ≈ 480 nm of the supernatant. The release amount of DOX at pH 7.4 in PBS is less than 5% after 24 h incubation (Figure S20a, Supporting Information); while only 3% of DOX and almost no Gd^{3+} ions are released from DOX&ICG/MLDH during the simulated blood circulation (Figure S20b and Table S1, Supporting Information), indicating a high stability of DOX&ICG/MLDH both in normal physiological environment and in blood circulation. However, 9.05% and 21.01% of DOX is released from DOX&ICG/MLDH at pH 6.5 and 5.0 over 8 h, respectively. We further investigated the release performance triggered by NIR laser irradiation. A pulse NIR irradiation of 1 min (808 nm, 1.5 W cm^{-2}) was performed during the release process (at time point 5, 20, 60 min), and a significantly increased drug release was obtained: 52.01% at pH = 7.4, 61.62% at pH = 6.5, and 82.37% at pH = 5.0 (Figure 3d). It should be noted that the release amount difference between pH = 7.4 and 6.5 is much less than that between pH = 6.5 and 5.0, owing to the partial dissolution of MLDH carrier at pH = 5.0.^[25] The fluorescence intensity of supernatant shows a gradual enhancement along with the prolongation of NIR irradiation time (Figure 3e), and the photograph of supernatant clearly illustrates the accumulated DOX release (Figure S21, Supporting Information). Moreover, the irradiation-controlled release of DOX is confirmed by the color change (from green to brown) of the DOX&ICG/MLDH suspension (Figure 3f; Video S1 in the Supporting Information). The results above verify that the photothermal effect of ICG can disrupt the interaction between DOX and ICG and thus induce the release of DOX.

Subsequently, we tested the intracellular drug release behavior. HepG2 cancer cells were incubated with DOX&ICG/MLDH for 6 h, and the weak red fluorescent signal in cytoplasm indicates the endocytosis of DOX&ICG/MLDH (Figure 4a). After the NIR light irradiation (808 nm, 3 min), an obviously increased fluorescence signal was observed in nuclei, demonstrating the release of DOX from DOX&ICG/MLDH and a delivery from cytoplasm into nuclei (Figure 4b). Previous studies reported that DOX needs to enter into the nuclei and bind with DNA to induce prominent cytotoxicity;^[53] the results prove that the MLDH nanosheets serve as a desirable nanocarrier for delivering chemotherapeutic drug with a stimulated release. Moreover, flow cytometer results also show an increased intracellular fluorescence intensity of DOX upon irradiation (Figure 4c), confirming the phototriggered intracellular release of DOX. Moreover, in view of the intrinsic photodynamic activity of ICG, the photodynamic capability of DOX&ICG/MLDH was examined by investigating the production of ROS in cancer cells, with 2,7-dichlorodihydrofluorescein diacetate as the probe.^[54] The results show DOX&ICG/MLDH induces a significantly enhanced ROS production in comparison with

control samples (DMEM, MLDH, DOX, DOX&ICG, and ICG) after NIR irradiation (Figure 4d,e).

Owing to the superior properties of the DOX&ICG/MLDH, we further investigated its cellular uptake pathway and in vitro therapeutic effect. It has been reported that the drug endocytosis process is mainly through the following three types of passway: a) macropinocytosis, b) caveolae-mediated endocytosis, and c) clathrin-mediated endocytosis.^[55] Figure 4f displays that the internalization was almost inhibited when the cells were cultured at 4 °C, indicating an energy-dependent-endocytosis process.^[56] Evaluations on cellular uptake of DOX&ICG/MLDH verify the passway of caveolae-mediated endocytosis. Subsequently, the anticancer performance of DOX&ICG/MLDH was investigated by in vitro tests. HepG2 cells were cultured with saline, MLDH, DOX, DOX/MLDH, ICG, ICG/MLDH, DOX&ICG, and DOX&ICG/MLDH, respectively with equivalent drug concentration ranging from 0.5 to 10 μg mL^{-1} for 24 h, washed thoroughly with PBS, and then irradiated with or without NIR light (808 nm, 1.5 W cm^{-2} , 3 min). The therapeutic efficacy in vitro was evaluated by the standard methyl thiazolyl tetrazolium assay. As shown in Figure 4g, in all cases, the anticancer effect enhances gradually with the dosage increment from 0.5 to 10 μg mL^{-1} . The half maximal inhibitory concentration (IC_{50}) of DOX&ICG/MLDH is 0.55 μg mL^{-1} , extremely smaller than that of DOX (9.07 μg mL^{-1}), DOX/MLDH (13.12 μg mL^{-1}), ICG (1.20 μg mL^{-1}), ICG/MLDH (0.96 μg mL^{-1}), and DOX&ICG (1.74 μg mL^{-1}), indicating a superior synergistic effect (between DOX and ICG) and ICG gives a predominant contribution. However, it is rather difficult to determine individual contribution of PDT or PTT (both originating from ICG) in DOX&ICG/MLDH, since the coexisting contribution of DOX cannot be excluded. The biocompatibility of MLDH nanosheets was also investigated. It is interesting that MLDH nanosheets display almost no cytotoxicity to four kinds of common cancer cells (U87mg, KB, HeLa, and HepG2 cells), even with a concentration as high as 500 μg mL^{-1} (Figures S22 and S23, Supporting Information). Moreover, DOX&ICG/MLDH, DOX/MLDH, and ICG/MLDH samples exhibit a less cytotoxicity to HepG2 cells compared with corresponding samples without MLDH (Figure S24, Supporting Information), indicating an enhanced biocompatibility with the presence of MLDH as drug carrier. For the purpose of visualizing the anticancer efficacy, HepG2 cells treated with 5 μg mL^{-1} of saline, MLDH, DOX, DOX/MLDH, ICG, ICG/MLDH, DOX&ICG, and DOX&ICG/MLDH upon NIR irradiation were stained with Calceinacetoxymethyl ester (Calcein-AM) and propidium iodide (Calcein-AM/PI) (Figure 4h). The results indicate the optimal anticancer capability of DOX&ICG/MLDH, which is consistent with the results of in vitro tests (Figure 4g).

In vivo distribution and tumor accumulation of DOX&ICG/MLDH in mice were investigated by using both in vivo NIRF and MR imaging. As the tumor volume reached 100 mm^3 , the mice were administered with an intravenous (i.v.) injection of DOX&ICG/MLDH and DOX&ICG respectively at the same dose (1 mg mL^{-1} , 200 μL) and then subjected to NIRF imaging. As shown in Figure 5a, in both cases, the ICG fluorescence was observed throughout the whole body after 2 h. For the mice treated with DOX&ICG/MLDH, a strong fluorescence signal in the tumor area increased gradually,

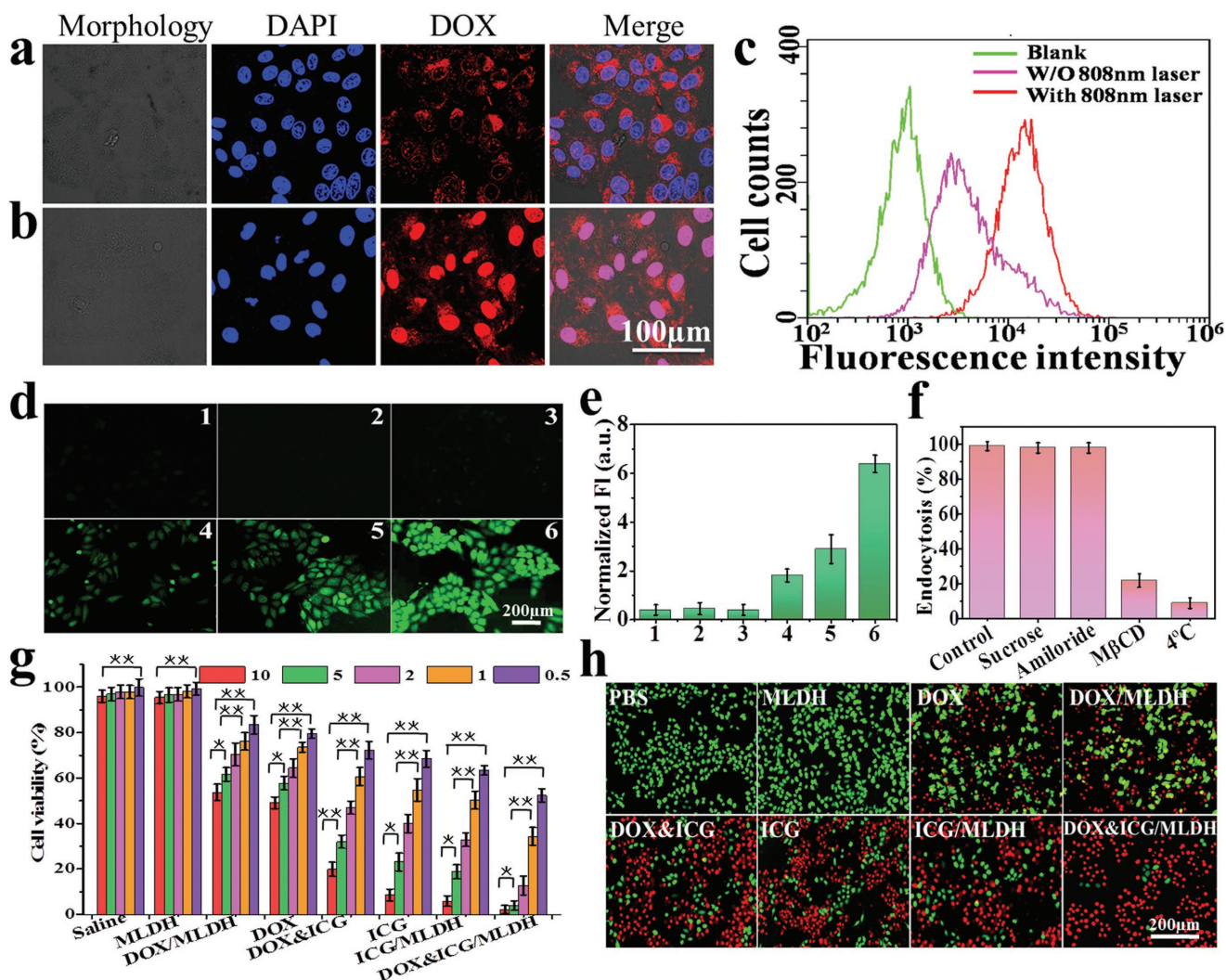


Figure 4. Confocal images of HepG2 cells incubated with DOX&ICG/MLDH: a) before and b) after NIR laser irradiation (808 nm, 1.5 W cm^{-2}). c) Intracellular fluorescence with and without NIR irradiation recorded by flow cytometer. d) Fluorescence images of ROS production in cancer cells treated with various drugs, and e) corresponding normalized fluorescence intensity: (1) DMEM, (2) MLDH, (3) DOX, (4) DOX&ICG, (5) ICG, and (6) DOX&ICG/MLDH. f) Inhibition of endocytosis treated with different inhibitors or at a low temperature (4°C). g) Viability of HepG2 cells in the presence of various drugs with different concentrations upon NIR irradiation ($*p < 0.05$, $**p < 0.01$) and h) corresponding Calcein-AM/PI staining images.

reached the highest level at 8 h, and maintained a significant intensity at 12 and 24 h. In contrast, for the mice treated with DOX&ICG, a rather weak ICG fluorescence was detected at 8 h, then decreased quickly and disappeared completely at 24 h. At 24 h post administration, the nude mice were sacrificed to obtain the tumor and normal organs for the ex vivo fluorescence imaging. The strongest fluorescence signal was observed at the tumor site compared with other normal organs (Figure S25a, Supporting Information), which was in agreement with the semiquantitative region-of-interest analysis (Figure S25b, Supporting Information). Thus, the results above indicate that the existence of MLDH nanosheets is responsible for the excellent passive targeted property and prolonged tumor retention time of DOX&ICG/MLDH. In vivo MRI was further employed to investigate the distribution of DOX&ICG/MLDH by virtue of a deep penetration and a high spatial resolution (Figure S26, Supporting Information).

After the intravenous injection of DOX&ICG/MLDH, the T_1 -weighted MR signal at tumor increased gradually and reached the strongest intensity at 8 h, in accordance with the results of in vivo NIRF imaging. The above results demonstrate that DOX&ICG/MLDH can serve as an effective dual-mode imaging agent for both in vivo NIRF and MR imaging, which gives clear-cut information for tumor accumulation after systemic administration.

Based on the selective accumulation of DOX&ICG/MLDH within tumor site, we further carried out an in vivo antitumor study to demonstrate the combination therapy of DOX&ICG/MLDH on mice bearing HepG2 tumor. The mice were divided into eight groups: (1) saline, (2) MLDH nanosheets, (3) DOX&ICG, (4) DOX&ICG/MLDH, (5) DOX/MLDH with irradiation, (6) DOX&ICG with irradiation, (7) ICG/MLDH with irradiation, and (8) DOX&ICG/MLDH with irradiation. The treated mice were i.v. injected with a total drug dose of 2.5 mg kg^{-1}

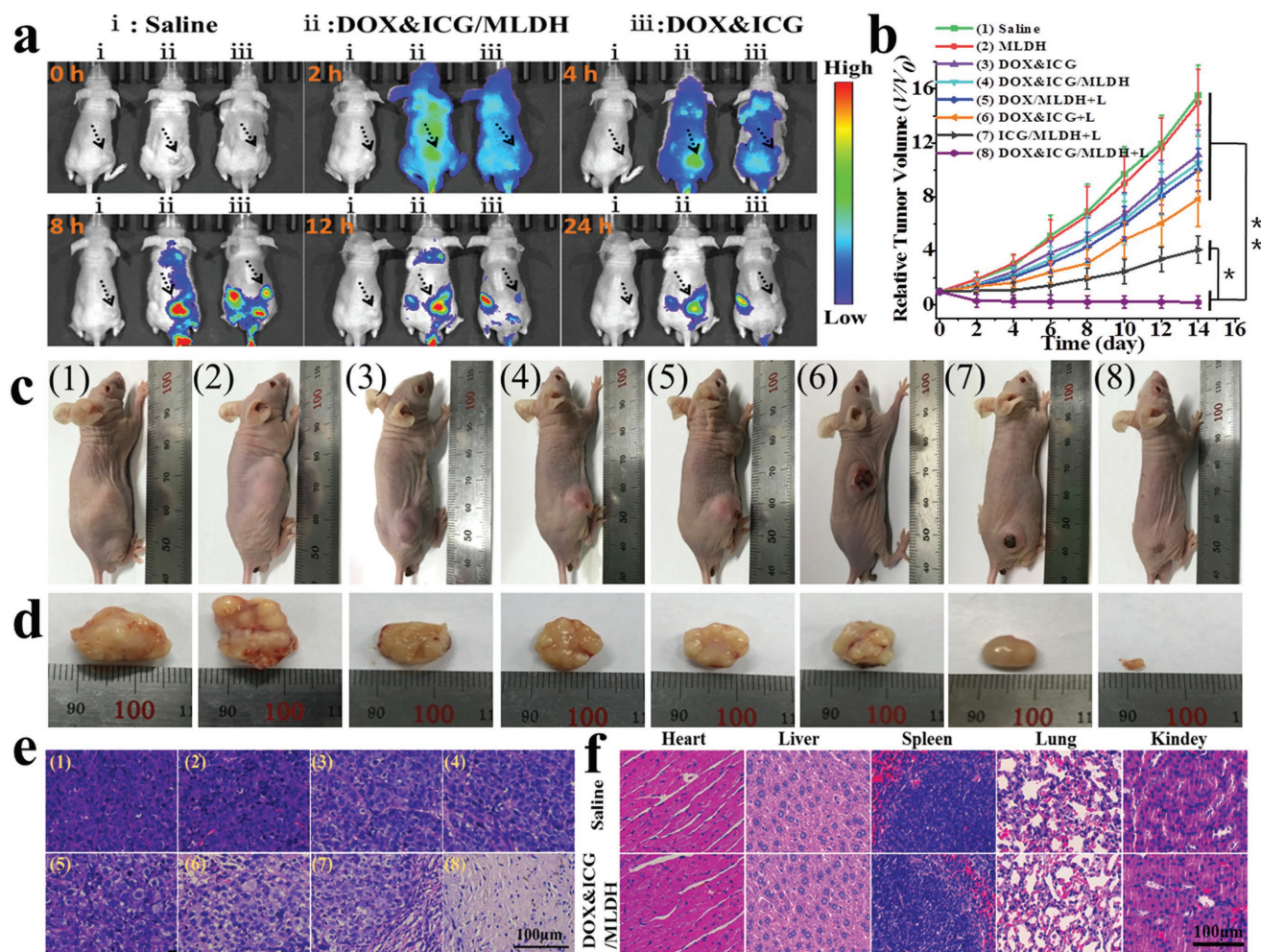


Figure 5. a) In vivo fluorescence imaging and biodistribution of nude mice bearing HepG2 tumors at different time points after intravenous injection of saline, DOX&ICG/MLDH, and DOX&ICG (the blank arrows point out the tumor location in mice). b) HepG2 tumor growth curves with various treatments (* $p < 0.05$, ** $p < 0.01$). c) Digital photographs of the mice on day 14 after various treatments shown in (b), and d) corresponding excised tumors. e) Representative histological images of the tumors collected on day 14. f) Histological images of the major organs collected on day 14 treated with saline and DOX&ICG/MLDH, respectively.

followed by an exposure to 808 nm laser (1.0 W cm^{-2}) for 3 min or no irradiation at 8 h post injection. The tumor volume was monitored within two weeks (Figure 5b). The saline and MLDH nanosheets show negligible tumor inhibition. The DOX&ICG and DOX&ICG/MLDH without irradiation as well as DOX/MLDH with irradiation partially inhibit the tumor growth due to the chemotherapy effectiveness; a significant therapeutic effect is obtained in the cases of DOX&ICG and ICG/MLDH with irradiation. Notably, the combination treatment with DOX&ICG/MLDH upon irradiation results in the most efficient inhibition of tumor growth compared with other control groups, indicating a remarkably enhanced in vivo synergistic therapeutic effect. The digital photos of the mice and corresponding excised tumors (Figure 5c,d) visually illuminate that the tumor size treated with DOX&ICG/MLDH plus irradiation is significantly smaller than the other groups. Hematoxylin and eosin (H&E) staining reveals that the tumor tissue treated with DOX&ICG/MLDH plus irradiation gives obvious necrosis;

while the control groups retain their normal morphology or show partial necrosis (Figure 5e). The largely improved therapeutic efficacy of DOX&ICG/MLDH in vivo can be attributed to a synergistic effect of chemo/PTT/PDT. Furthermore, to investigate the metabolism and degradation of DOX&ICG/MLDH in vivo, Mg concentrations in the major organs of mice were tested using inductively coupled plasma mass spectrometry (Figure S27a, Supporting Information). The results showed that high levels of Mg element were found in the tumor, as well as liver, spleen, and lung within the first 8 h, which indicated that MLDH was accumulated via reticuloendothelial systems (RES) absorption. Subsequently, Mg level decreased gradually with the extension of time in all organs. Moreover, Mg concentration in both feces and urine reached maximum at 8 h post administration and then decreased with time (Figure S27b, Supporting Information). Therefore, the above results confirm that DOX&ICG/MLDH is accumulated via RES and further metabolized by the way of feces and urine, indicating its potential

clinical application. Moreover, no significant decrease in mice weight for each group was found during the treatment, demonstrating no obvious side effect (Figure S28, Supporting Information). In addition, we evaluated the in vivo toxicity of MLDH nanosheets with i.v. injection of MLDH (200 μ L, 10 mg kg^{-1}): the blood biochemistry as well as the liver and kidney function markers was all within their normal ranges relative to healthy mice (Figure S29, Supporting Information). Moreover, the H&E analysis of major organs (heart, liver, spleen, lung, and kidney) (Figure 5f) shows no significant damage in DOX&ICG/MLDH and saline group, indicating a satisfactory safety of MLDH nanosheets used in cancer theranostics. Compared with other 2D nanomaterials, the abundant surface hydroxyl groups and electropositivity of MLDH nanosheets provide favorable binding sites, accounting for the ultrahigh drug loading (as high as 797.36% in this work). In addition, LDHs has been commercially used as the main component for antacid or anti-pepsin agent with a high security,^[57] which would guarantee its potential application in cancer theranostics.

In summary, DOX&ICG/MLDH has been demonstrated as a smart and versatile “all-in-one” platform with inherent NIRF/MR imaging as well as synergistic chemo/PTT/PDT therapy. MLDH nanosheets as drug carrier show an unprecedented high loading of DOX&ICG (797.36%), which is the highest LC level at nearly 100% of EE compared with previously reported 2D drug carriers. The intrinsic NIRF/MR imaging ability of DOX&ICG/MLDH enables a noninvasive real-time visualization of the distribution profiles at the tumor sites, which favors a precise diagnosis and efficient treatment. In addition, in vivo therapeutic evaluations in HepG2 tumor-bearing mice demonstrate a complete ablation of tumor by virtue of the synergistic chemo/PTT/PDT effect while the toxicity studies with a large dose of MLDH nanosheets give scarcely any in vivo toxicity. Therefore, the theranostic system based on MLDH nanosheets will open new perspectives in the design of multifunctional nanomedicine materials for the future clinical cancer diagnosis and treatment.

Supporting Information

Supporting Information is available online from the Wiley Online Library or from the author.

Acknowledgements

This work was supported by the National Natural Science Foundation of China (NSFC), the 973 Program (Grant No. 2014CB932103), Beijing Natural Science Foundation (2174082), the Fundamental Research Funds for the Central Universities (buctylkxj01), and Ten Diseases & Ten Drugs' Project of Beijing Municipal Science & Technology Commission (No. Z171100001717009). Male Balb/c mice were purchased from Beijing Vital River Laboratory Animal Technology Co., Ltd and used under protocols approved by the China–Japan Friendship Hospital Animal Research Center.

Conflict of Interest

The authors declare no conflict of interest.

Keywords

cancer theranostics, drug loading, layered double hydroxides, monolayer nanosheets, 2D nanomaterials

Received: December 18, 2017

Revised: January 24, 2018

Published online:

- [1] X. Qian, J. Liu, L. Fu, J. Li, *Science* **2014**, *346*, 1344.
- [2] Z. Liu, L. Ma, G. Shi, W. Zhou, Y. Gong, S. Lei, X. Yang, J. Zhang, J. Yu, K. P. Hackenberg, A. Babakhani, J. C. Idrobo, R. Vajtai, J. Lou, P. M. Ajayan, *Nat. Nanotechnol.* **2013**, *8*, 119.
- [3] S. Wang, X. Li, Y. Chen, X. Cai, H. Yao, W. Gao, Y. Zheng, X. An, J. Shi, H. Chen, *Adv. Mater.* **2015**, *27*, 2775.
- [4] G. Y. Lee, W. P. Qian, L. Wang, Y. A. Wang, C. A. Staley, M. Satpathy, S. Nie, H. Mao, L. Yang, *ACS Nano* **2013**, *7*, 2078.
- [5] S. S. Chou, B. Kaehr, J. Kim, B. M. Foley, M. De, P. E. Hopkins, J. Huang, C. J. Brinker, V. P. Dravid, *Angew. Chem., Int. Ed.* **2013**, *52*, 4160.
- [6] S. Y. Qin, J. Feng, L. Rong, H. Z. Jia, S. Chen, X. J. Liu, G. F. Luo, R. X. Zhuo, X. Z. Zhang, *Small* **2014**, *10*, 599.
- [7] H. J. Yoon, T. H. Kim, Z. Zhang, E. Azizi, T. M. Pham, C. Paoletti, J. Lin, N. Ramnath, M. S. Wicha, D. F. Hayes, D. M. Simeone, S. Nagrath, *Nat. Nanotechnol.* **2013**, *8*, 735.
- [8] K. Kalantar-Zadeh, J. Z. Ou, T. Daeneke, M. S. Strano, M. Pumera, S. L. Gras, *Adv. Funct. Mater.* **2015**, *25*, 5086.
- [9] T. T. Tran, K. Bray, M. J. Ford, M. Toth, I. Aharonovich, *Nat. Nanotechnol.* **2016**, *11*, 37.
- [10] F. Xia, H. Wang, Y. Jia, *Nat. Commun.* **2014**, *5*, 4458.
- [11] X. R. Song, X. Wang, S. X. Yu, J. Cao, S. H. Li, J. Li, G. Liu, H. H. Yang, X. Chen, *Adv. Mater.* **2015**, *27*, 3285.
- [12] T. Liu, C. Wang, X. Gu, H. Gong, L. Cheng, X. Shi, L. Feng, B. Sun, Z. Liu, *Adv. Mater.* **2014**, *26*, 3433.
- [13] L. Cheng, J. Liu, X. Gu, H. Gong, X. Shi, T. Liu, C. Wang, X. Wang, G. Liu, H. Xing, W. Bu, B. Sun, Z. Liu, *Adv. Mater.* **2014**, *26*, 1886.
- [14] W. Chen, J. Ouyang, H. Liu, M. Chen, K. Zeng, J. Sheng, Z. Liu, Y. Han, L. Wang, J. Li, L. Deng, Y. N. Liu, S. Guo, *Adv. Mater.* **2017**, *29*, 1603864.
- [15] M. Chen, S. Tang, Z. Guo, X. Wang, S. Mo, X. Huang, G. Liu, N. Zheng, *Adv. Mater.* **2014**, *26*, 8210.
- [16] X. Zhao, C. X. Yang, L. G. Chen, X. P. Yan, *Nat. Commun.* **2017**, *8*, 14998.
- [17] L. Zhang, J. Xia, Q. Zhao, L. Liu, Z. Zhang, *Small* **2010**, *6*, 537.
- [18] A. Falin, Q. Cai, E. J. G. Santos, D. Scullion, D. Qian, R. Zhang, Z. Yang, S. Huang, K. Watanabe, T. Taniguchi, M. R. Barnett, Y. Chen, R. S. Ruoff, L. H. Li, *Nat. Commun.* **2017**, *8*, 15815.
- [19] Q. Han, X. Wang, X. Jia, S. Cai, W. Liang, Y. Qin, R. Yang, C. Wang, *Nanoscale* **2017**, *9*, 5927.
- [20] C. Zhu, Z. Zeng, H. Li, F. Li, C. Fan, H. Zhang, *J. Am. Chem. Soc.* **2013**, *135*, 5998.
- [21] W. Yin, L. Yan, J. Yu, G. Tian, L. Zhou, X. Zheng, X. Zhang, Y. Yong, J. Li, Z. Gu, Y. Zhao, *ACS Nano* **2014**, *8*, 6922.
- [22] P. J. Sideris, U. G. Nielsen, Z. Gan, C. P. Grey, *Science* **2008**, *321*, 113.
- [23] G. Hu, D. O'Hare, *J. Am. Chem. Soc.* **2005**, *127*, 17808.
- [24] G. R. Williams, A. I. Khan, D. O'Hare, in *Layered Double Hydroxides*, Vol. 119, (Eds.: X. Duan, D. G. Evans), Springer, Berlin/Heidelberg, Germany **2006**, p. 161.
- [25] Q. Wang, D. O'Hare, *Chem. Rev.* **2012**, *112*, 4124.
- [26] Y. Dou, S. Zhang, T. Pan, S. Xu, A. Zhou, M. Pu, H. Yan, J. Han, M. Wei, D. G. Evans, X. Duan, *Adv. Funct. Mater.* **2015**, *25*, 2243.
- [27] D. Chimene, D. L. Alge, A. K. Gaharwar, *Adv. Mater.* **2015**, *27*, 7261.

- [28] R. Liang, R. Tian, L. Ma, L. Zhang, Y. Hu, J. Wang, M. Wei, D. Yan, D. G. Evans, X. Duan, *Adv. Funct. Mater.* **2014**, *24*, 3144.
- [29] B. Li, Z. Gu, N. Kurniawan, W. Chen, Z. P. Xu, *Adv. Mater.* **2017**, *29*, 1700373.
- [30] L. Wang, H. Xing, S. Zhang, Q. Ren, L. Pan, K. Zhang, W. Bu, X. Zheng, L. Zhou, W. Peng, Y. Hua, J. Shi, *Biomaterials* **2013**, *34*, 3390.
- [31] D. Li, Y. T. Zhang, M. Yu, J. Guo, D. Chaudhary, C. C. Wang, *Biomaterials* **2013**, *34*, 7913.
- [32] R. Tian, D. Yan, C. Li, S. Xu, R. Liang, L. Guo, M. Wei, D. G. Evans, X. Duan, *Nanoscale* **2016**, *8*, 9815.
- [33] W. Tao, X. Zhu, X. Yu, X. Zeng, Q. Xiao, X. Zhang, X. Ji, X. Wang, J. Shi, H. Zhang, L. Mei, *Adv. Mater.* **2017**, *29*, 1603276.
- [34] B. Tian, C. Wang, S. Zhang, L. Feng, Z. Liu, *ACS Nano* **2011**, *5*, 7000.
- [35] Y. Chen, D. Ye, M. Wu, H. Chen, L. Zhang, J. Shi, L. Wang, *Adv. Mater.* **2014**, *26*, 7019.
- [36] M. Fojtů, X. Chia, Z. Sofer, M. Masařík, M. Pumera, *Adv. Funct. Mater.* **2017**, *27*, 1701955.
- [37] Q. Weng, B. Wang, X. Wang, N. Hanagata, X. Li, D. Liu, X. Wang, X. Jiang, Y. Bando, D. Golberg, *ACS Nano* **2014**, *8*, 6123.
- [38] T. Jiang, W. Sun, Q. Zhu, N. A. Burns, S. A. Khan, R. Mo, Z. Gu, *Adv. Mater.* **2015**, *27*, 1021.
- [39] D. Frenkel, B. Smit, *Understanding Molecular Simulation: from Algorithms to Applications*, Vol. 1, Academic Press, San Diego, CA, USA **2001**.
- [40] L. Li, R. Z. Ma, Y. Ebina, N. Iyi, T. Sasaki, *Chem. Mater.* **2005**, *17*, 4386.
- [41] Z. Liu, R. Ma, M. Osada, N. Iyi, Y. Ebina, K. Takada, T. Sasaki, *J. Am. Chem. Soc.* **2006**, *128*, 4872.
- [42] T. Sasaki, M. Watanabe, *J. Am. Chem. Soc.* **1998**, *120*, 4682.
- [43] Z. Zhu, X. Wang, T. Li, S. Aime, P. J. Sadler, Z. Guo, *Angew. Chem., Int. Ed.* **2014**, *53*, 13225.
- [44] F. Liu, X. He, H. Chen, J. Zhang, H. Zhang, Z. Wang, *Nat. Commun.* **2015**, *6*, 8003.
- [45] Y. Li, T. Y. Lin, Y. Luo, Q. Liu, W. Xiao, W. Guo, D. Lac, H. Zhang, C. Feng, S. Wachsmann-Hogiu, J. H. Walton, S. R. Cherry, D. J. Rowland, D. Kukis, C. Pan, K. S. Lam, *Nat. Commun.* **2014**, *5*, 4712.
- [46] M. Zheng, C. Yue, Y. Ma, P. Gong, P. Zhao, C. Zheng, Z. Sheng, P. Zhang, Z. Wang, L. Cai, *ACS Nano* **2013**, *7*, 2056.
- [47] H. Wang, P. Agarwal, S. Zhao, J. Yu, X. Lu, X. He, *Nat. Commun.* **2015**, *6*, 10081.
- [48] L. Martino, A. Virno, B. Pagano, A. Virgilio, S. Di Micco, A. Galeone, C. Giancola, G. Bifulco, L. Mayol, A. Randazzo, *J. Am. Chem. Soc.* **2007**, *129*, 16048.
- [49] A. M. Spuches, D. E. Wilcox, *J. Am. Chem. Soc.* **2008**, *130*, 8148.
- [50] Y. Zheng, S. You, C. Ji, M. Yin, W. Yang, J. Shen, *Adv. Mater.* **2016**, *28*, 1375.
- [51] Z. Hou, Y. Zhang, K. Deng, Y. Chen, X. Li, X. Deng, Z. Cheng, H. Lian, C. Li, J. Lin, *ACS Nano* **2015**, *9*, 2584.
- [52] Z. Yaari, D. da Silva, A. Zinger, E. Goldman, A. Kajal, R. Tshuva, E. Barak, N. Dahan, D. Hershkovitz, M. Goldfeder, J. S. Roitman, A. Schroeder, *Nat. Commun.* **2016**, *7*, 13325.
- [53] P. Liu, H. Cheng, S. Santiago, M. Raeder, F. Zhang, A. Isabella, J. Yang, D. J. Semaan, C. Chen, E. A. Fox, N. S. Gray, J. Monahan, R. Schlegel, R. Beroukhim, G. B. Mills, J. J. Zhao, *Nat. Med.* **2011**, *17*, 1116.
- [54] C. Seidl, J. Ungelenk, E. Zittel, T. Bergfeldt, J. P. Sleeman, U. Schepers, C. Feldmann, *ACS Nano* **2016**, *10*, 3149.
- [55] S. Li, K. Wang, Y. Shi, Y. Cui, B. Chen, B. He, W. Dai, H. Zhang, X. Wang, C. Zhong, *Adv. Funct. Mater.* **2016**, *26*, 2715.
- [56] C. Wang, H. Xu, C. Liang, Y. Liu, Z. Li, G. Yang, L. Cheng, Y. Li, Z. Liu, *ACS Nano* **2013**, *7*, 6782.
- [57] D.-H. Park, G. Choi, J.-H. Choy, in *Photofunctional Layered Materials*, Vol. 166 (Eds.: D. Yan, M. Wei), Springer International Publishing, Cham, Switzerland **2015**, p. 137.